The influence of microstructure on the sintering process in crystalline metal powders investigated by positron lifetime spectroscopy: II. Tungsten powders with different powder-particle sizes

1999 J. Phys.: Condens. Matter 11 1787

(http://iopscience.iop.org/0953-8984/11/7/010)

J. Phys.: Condens. Matter **11** (1999) 1787–1806. Printed in the UK PII: S0953-8984(99)80632-8

The influence of microstructure on the sintering process in crystalline metal powders investigated by positron lifetime spectroscopy: II. Tungsten powders with different powder-particle sizes

T E M Staab†‖, R Krause-Rehberg†, B Vetter‡, B Kieback‡, G Lange§ and P Klimanek§

† Martin-Luther Universität Halle-Wittenberg, Fachbereich Physik, Friedemann-Bach-Platz 6, D-06108 Halle/Saale, Germany
‡ Technische Universität Dresden, Institut für Werkstoffwissenschaften, Momsenstraße 13, D-01062 Dresden, Germany
§ Bergakademie TU Freiberg, Institut für Metallkunde, Zeunerstraße 5, D-09599 Freiberg, Germany

Received 3 January 1997, in final form 4 November 1998

Abstract. Compacts of tungsten powder with five different powder-particle sizes (from 0.4 μm to 75 μm) are subjected to pressureless sintering. We investigate the change in microstructure during the sintering process by positron lifetime spectroscopy. So as to be able to distinguish between defects having the same positron lifetime, we investigate their kinetics when the sample is annealed. In particular, we consider the annealing out of vacancy clusters after low-temperature electron irradiation, as well as recovery and recrystallization of a tungsten sheet, in as-manufactured form. Making measurements on uncompacted powder, we find an increasing fraction of positrons annihilating in surface states with decreasing powder-particle size. The powder-particle and grain sizes (influencing the x-ray domain size) are monitored additionally by means of metallography and x-ray diffraction. We find that all of the methods give results in agreement with each other. The small grain sizes at lower temperature, about one fifth of the powder-particle size, cause positrons to annihilate at grain boundaries, leading to vacancy-cluster-like signals. At the intensive-shrinkage stage, there are certainly contributions from different shrinkage mechanisms. The observed shrinkage rates can be explained by *Coble* creep. It is possible that dislocations also play a role as vacancy sources and sinks, since the intensive-shrinkage stage occurs in a temperature region wherein recrystallization takes place.

1. Introduction

Sintered tungsten is an important intermediate product for the production of lamp filaments. For optimization of the production process, it would be advantageous to obtain a deeper insight into the mechanisms governing the sintering process, e.g. by obtaining estimates for the shrinkage rate. Up to now, there have been several such mechanisms under consideration for powders used in technical applications. Since one mechanism is based on defect-induced diffusion, we try to detect defects on an atomic scale using positron lifetime spectroscopy (POLIS), i.e. we try to get information about the parameters influencing the sintering process.

‖ Present address: Helsinki University of Technology, Laboratory of Physics, PO Box 1100, FIN-02015 HUT, Finland.

0953-8984/99/071787+20$19.50

Positrons can be used to detect different lattice defects separately when using lifetime spectroscopy. Dislocations, monovacancies, vacancy clusters, and interfaces (small- and large-angle grain boundaries), as well as internal surfaces (voids), are possible positron traps in one-component metallic systems (see the comprehensive discussions in part I [6] and [1]). However, there is a problem, in that different kinds of defect give similar signals: monovacancies in tungsten should have positron lifetimes of 167–180 ps [2], while dislocations and small-angle grain boundaries are expected to have positron lifetimes that are nearly the same (about 153 ps). Vacancy clusters (positron lifetimes: 200–450 ps) and large-angle grain boundaries can both have positron lifetimes of about 300 ps [1]. Finally, positron lifetimes at metallic surfaces are, according to theoretical and experimental results, 450–650 ps (see references [1, 3, 4] and references therein).

In view of these ambiguities, it is crucial to determine grain sizes inside powder particles, as well as the powder-particle sizes themselves, by metallographic methods. Which kinds of defect may be detected at certain temperatures can be determined by using results of the Monte Carlo simulation of the positron diffusion and knowledge of the annealing kinetics determined by complementary investigations (of the annealing out of radiation-induced defects, i.e. vacancies, and vacancy clusters, and the annealing out of defects created by plastic deformation). We investigated plastically deformed and electron-irradiated samples, even though these were discussed in the literature in the 1970s and early 1980s; at that time the experimental equipment was not so well developed, and only recently has a comprehensive study based on multi-component analysis of lifetime spectra appeared [5]. Hence, the decomposition of lifetime spectra for plastically deformed and electron-irradiated samples gives qualitatively new information. Furthermore, the investigations serve to calibrate the spectrometer, i.e. to make the determination of the positron lifetimes in defects (e.g. dislocations) more accurate.

A further important question is that of whether the defects are evenly distributed. If they are, this would allow the application of the standard trapping model. If the defects are inhomogeneously distributed—e.g. with a defect-free interior of the grains, with positrons trapped at the boundaries—the effect of diffusion has to be incorporated into the trapping model [1].

In part I we investigated the sintering of compacts of copper powders. In the case of compacts of tungsten powder, considered here (part II), special attention was paid to the effect of different powder-particle sizes, which should result in different driving forces for sintering. For positron annihilation, this should lead to different contributions from the surface-state annihilation because of such small particles being considered here.

One has to distinguish between sintering with and without external pressure. We consider here exclusively pressureless sintering (just called sintering in the following). 'Sintering' means heating a compact up to $4/5$ of its melting temperature, where the observed shrinkage is a pressureless process. The driving force is caused by the difference in free energy between the initial and final state. This difference is realized in one-phase systems by reducing the fraction of surfaces and interfaces. The morphology and microstructure of the powder† as well as the powder-particle sizes determine the shrinkage rate. Furthermore, the shrinkage rate depends on process parameters like the green density, heating rate, and sintering temperature. By *contact boundary* we mean the inter-particle contact evolving during sintering from a pure pressing contact to an irregular grain boundary.

Different shrinkage mechanisms are proposed: diffusional creep, dislocation creep, and

† 'Morphology' includes powder-particle sizes and shape, while the microstructure is determined by grain and subgrain sizes, dislocation density, etc.

viscous flow (only in amorphous materials). The corresponding equations for the shrinkage rate are discussed in part I [6] (or see [7] and [8]). The observed macroscopic shrinkage must be caused by material transport on an atomic scale, which should be realized by a vacancy mechanism. The controversial question is that of what the sources and sinks are. The candidates discussed are large- and small-angle grain boundaries (Nabarro–Herring creep), dislocations (Kosevic creep), and dissolving vacancy clusters leading to excess vacancies. Furthermore, the transport can be realized via grain boundary diffusion (Coble creep) or by dislocations via pipe diffusion.

Usually, the prevailing part of the shrinkage is realized while heating the sample, i.e. when recrystallization is complete and grain growth is starting at higher temperatures. This will be different for compacts of tungsten powder, investigated here, due to the low homologous sintering temperature.

Since the powder-particle size determines the driving force for pressureless sintering, one has to obtain a certain value for the *effective powder-particle size*, i.e. excluding effects from agglomeration and dendritic morphology. Furthermore, one should not *a priori* neglect the inner structure of the powder particles (more or less assuming them to be single crystals). Nabarro–Herring and Coble creep could seem to be inappropriate for describing the observed high shrinkage rates. Considering an effective powder-particle size and the inner microstructure, a data analysis will lead to shrinkage rates of the same order of magnitude as the observed ones [1, 6].

The outline of this article is as follows. Section 2 contains a description of the experimental set-up and sample treatment. In section 3 we present the results of our investigations, which are then discussed in section 4. Finally we present our conclusions in section 5.

2. Experiments

The tungsten powder was produced by the Hermann C Stark Company, Berlin (Germany). The different-sized powder particles possess different microstructures (dislocations, grain sizes) due to the different production processes, i.e. the different temperatures at which the reduction of the tungsten oxide is performed. Due to the preferred different growth types of nucleation centres, smaller powder-particle sizes are produced at lower temperatures and larger particle sizes at higher temperatures. This leads to states for smaller powder particles far from equilibrium.

During the pressing, we applied a uniaxial pressure of 700 MPa to samples of all powder-particle sizes. Those with smaller particle sizes showed more adhesion; i.e. better mechanical stability of the compact was achieved.

For POLIS measurements, the samples were heated up to the appropriate temperatures at a heating rate of 50 K min^{-1} and then cooled in the furnace. These samples were used later for x-ray diffraction and metallographic studies, in which the samples were first ground, and then polished, and finally we performed a grain boundary etching. Pictures were then taken using a scanning electron microscope (SEM), due to its better resolution. ^{22}Na is used as the positron source; the radioactive salt is placed between two thin (2 μm) Al foils. The spectra are taken in a source–sample arrangement where the source is placed between two identical samples (in a sandwich). We use a standard fast–fast coincidence lifetime set-up with plastic scintillators (see [1] for a detailed description). The linear shrinkage was measured *in situ* by a high-temperature dilatometer at the TU Dresden at a heating rate of 30 K min^{-1}. The shrinkage rate is then calculated by taking the time derivative of the linear shrinkage.

The sintering temperature of 1650 °C corresponds to a homologous temperature $T_\mathrm{S} = 0.52\,T_\mathrm{M}$. Since the melting point of pure tungsten is $T_\mathrm{M} = 3683$ K (3410 °C), recrystallization

is expected to occur at $T_R \approx 0.4\ T_M = 1473$ K (1200 °C).

Due to the difficulty of cold rolling tungsten, we took as the deformed state just the manufactured (hot-rolled) form, and hence we performed the measurement on a tungsten sheet in as-produced form. Rolling of tungsten sheets is usually performed at 1300 °C.

3. Results

To get some information about the influence of the powder production process on the microstructure and lattice defects, we made measurements on the uncompacted powders, and found that the smaller the powder-particle size, the higher the defect density in the powder particles, and hence the higher the fraction of positrons annihilating, probably at grain boundaries and in surface states. This will be comprehensively discussed in section 3.2.3.

The maximum of the shrinkage rate is reached at 1350 °C during the heating of the samples with the smallest powder-particle size ($\bar{L}_P = 0.4\ \mu$m), and at 1650 °C, i.e. at the start of the isothermal sintering range, for samples of powder-particle size $\bar{L}_P = 1.8\ \mu$m. Some shrinkage is observed during the heating as well. The maximum is not so pronounced as for the samples with the smallest particle size. For compacts with a powder-particle size of 3.8 μm, measurable shrinkage was noticed only at 1650 °C, i.e. in the isothermal sintering range, while compacts with a 23 μm powder-particle size did not show any significant shrinkage at the temperature of the experiment.

3.1. Metallographic studies

The sequence of pictures in figures 1 and 2 show different stages of the sintering process for the samples with the two smallest powder-particle sizes, since the two with larger powder-particle sizes did not show any significant macroscopic shrinkage at the low homologous sintering temperature (1650 °C). Due to poor mechanical stability, the samples sintered at lower

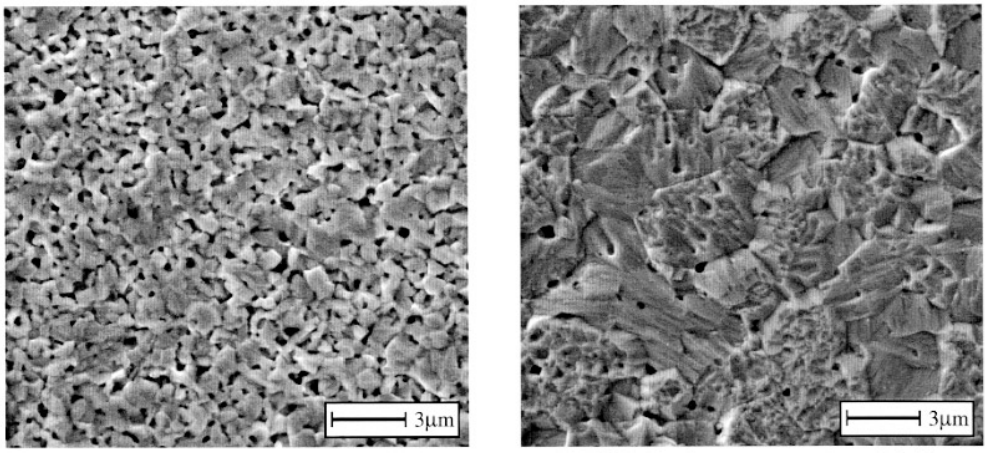

Figure 1. SEM pictures showing compacts of tungsten powder ($\bar{L}_P = 0.4\ \mu$m) after heat treatment to the temperatures given. The pictures show the samples after grinding, polishing, and grain boundary etching. The temperature and density at the indicated stage of sintering are given below each picture.

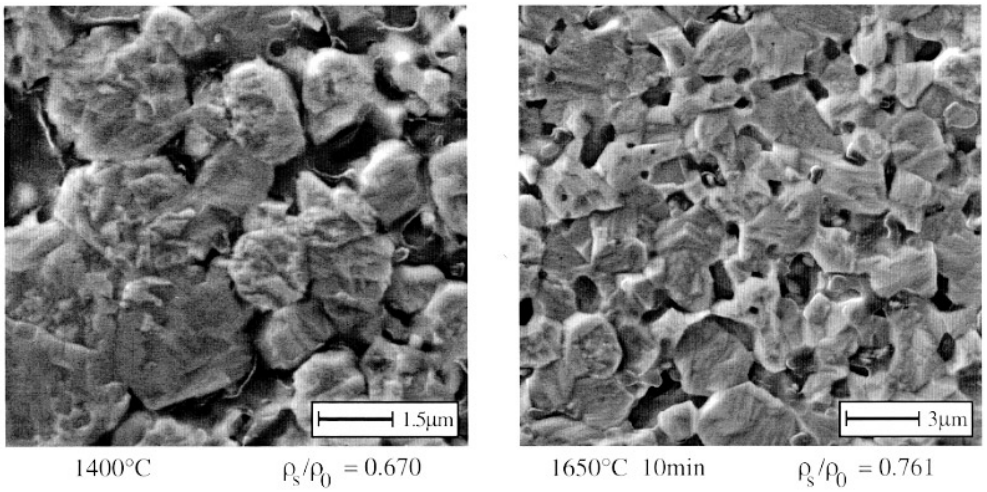

Figure 2. SEM pictures showing compacts of tungsten powder ($\bar{L}_P = 1.8\,\mu$m) after heat treatment to the given temperatures. The pictures show the samples after grinding, polishing, and grain boundary etching. The temperature and density at the indicated stage of sintering are given below each picture.

Table 1. Green densities (ρ_g) and densities after sintering at 1650 °C for 30 min (ρ_s); for compacts with different powder-particle sizes $\bar{L}_P$. The pressure applied was 700 MPa in every case, and the heating rate under H_2 was 50 K min^{-1}. The relative shrinkage increases with decreasing powder-particle size.

$\bar{L}_P$ (μm)	ρ_g/ρ_0	ρ_s/ρ_0
0.4	0.53	0.96
1.8	0.64	0.83
3.8	0.68	0.84
23	0.73	0.74

temperatures, i.e. below 1300 °C, were difficult to prepare for microstructure investigations. Hence one could obtain only pictures showing individual powder particles.

SEM pictures (not shown here) reveal that even in the case of the smallest powder particles each individual powder particle seems to consist of one or several crystallites: for $\bar{L}_P = 0.4\,\mu$m: $\bar{L}_G \approx 100$ nm, and for $\bar{L}_P = 1.8\,\mu$m: $\bar{L}_G \approx 500$ nm. Note that it is appropriate to speak of individual powder particles only at lower temperatures, i.e. below 1400 °C.

The astonishing fact is that in the case of the smallest particle size, nearly poreless material, i.e. having 0.96 of the theoretical maximum density, is obtained as a result of a heat treatment in which the maximum temperature is only 0.52 T_M (see table 1 and figure 1). And even in the case of the next-larger powder-particle size $\bar{L}_P = 1.8\,\mu$m, significant shrinkage is noticed and the microstructure changes completely (see table 1 and figure 2). From figures 2 and 1 it is obvious that significant grain growth accompanies shrinkage—especially for the smallest powder-particle size.

3.2. Defect structures—positron lifetime measurements

The values for positron lifetimes in the bulk and in vacancies from the literature are given in table 2.

Table 2. Positron data for tungsten according to Schaefer *et al* and de Vries, and those obtained from our investigations. Here the symbols mean the lifetimes in the bulk (τ_b), in dislocations (τ_{disl}), in thermal vacancies with sample temperature 2900 K (τ_v^{therm}), in irradiation-induced vacancies at sample temperature 300 K (τ_v^{irrad}), at grain boundaries (τ_{GB}), and at surfaces (τ_{surf}).

	Schaefer [2]	de Vries [10]	This work
τ_b (ps)	105	—	103 ± 2
τ_{disl} (ps)	—	150	153 ± 2
τ_v^{therm} (ps)	149	—	—
τ_v^{irrad} (ps)	180	—	> 165
τ_{GB} (ps)	—	—	315 ± 30
τ_{surf} (ps)	—	—	615 ± 40

In tungsten, vacancies in thermal equilibrium seem not to be detectable by means of positrons up to 2000 K [2]. As the trapping coefficient for dislocations, we take, due to the lack of reliable data for tungsten, the value determined for copper and nickel, i.e. $\mu_{disl} = 1.1 \pm 0.2$ cm^{-2} s^{-1}. For the positron diffusion coefficient in tungsten, we assume $D_+ = 1.4$ cm^2 s^{-1} (experiments lead to a value of $D_+ = 1.4$ cm^2 s^{-1} [11], while theory gives $D_+ = 1.26$ cm^2 s^{-1} [3] which is in fair agreement with most recent measurements on the similar refractory metal Mo, giving $D_+ = 1.1 \pm 0.1$ cm^2 s^{-1} [12]).

3.2.1. Recovery after plastic deformation. Since it is difficult to deform tungsten by cold rolling, we took as the deformed state just the manufactured (hot-rolled) one, and carried out an annealing experiment on this.

It is known from electrical resistivity measurements for heavily plastically deformed tungsten that stage III annealing is observed between 300 and 500 °C [13, 14]. This annealing stage is attributed to vacancy migration. Stage IV, between 500 and 1000 °C, is not so pronounced, and it was questionable to which kinds of defect it should be attributed. Recrystallization is observed above 1000 °C (stage V) for zone-refined material [13,14], while the usually accepted recrystallization temperature is higher (see section 2).

The lifetime analysis shows for lower temperatures complete trapping into defects. In the two-component spectrum, the first lifetime obtained, $\tau_2 = 165$ ps, could reflect annihilation at monovacancies or dislocations or any kind of combination of the two, while the second lifetime component obtained, $\tau_3 \approx 350$ ps, certainly reflects positron capture in vacancy clusters according to the annealing kinetics described in section 3.2.2. From the annealing curve, we can see that monovacancies seem to become mobile above 400 °C, the temperature at which vacancy clusters—already present in the as-produced state—start to coarsen, and their intensity rises slightly at about 500 °C (see figure 3). The average lifetime rises slightly as well. The cluster intensity goes down at higher temperatures again, while further coarsening is observed, indicated by an increasing lifetime τ_3. At 1000 °C, nearly all vacancy clusters have vanished, i.e. are no longer more visible by means of positrons—meaning that their density has dropped below the detection limit (see [1]). Above 1100 °C, only a dislocation signal with a lifetime of about 153 ps remains. At 1450 °C, we reached the highest possible temperature for our furnace. The recrystallization was not complete at this temperature.

3.2.2. Recovery after quenching and electron irradiation. It is known from previous studies that after irradiation with 2.9 MeV electrons at 280 K with a dose of 6×10^{22} m^{-2} there is only a vacancy signal (a single-lifetime spectrum; lifetimes: about 180 ps) detected up to about 700 K (430 °C) [15]. Thereafter, clustering is observed where vacancy agglomerates

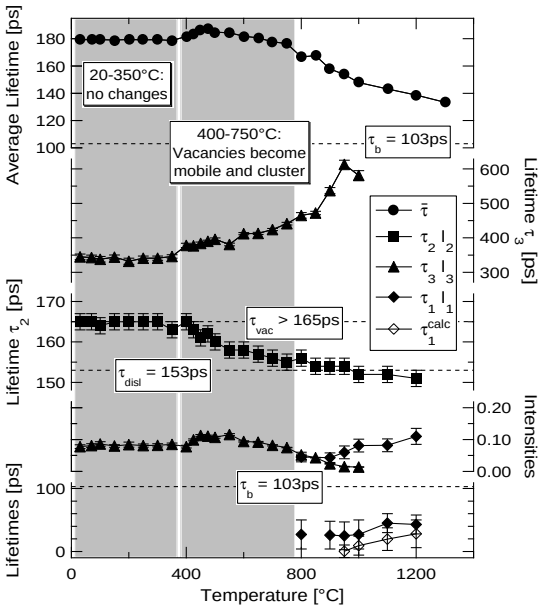

Figure 3. Annealing of as-produced tungsten slides of purity 3N5; the upper part gives the change of the average lifetime with annealing temperature, while the lower part shows a decomposition of the spectra.

first coarsen and then anneal in the temperature range from 850 to 1350 K (580–1080 °C). The bulk lifetime is obtained again at about 1370 K, i.e. 1100 °C [15].

The onset of vacancy migration at about 750 K is observed after quenching with electrical resistometry as well [16]. The authors of [16] obtained a vacancy migration enthalpy of 1.78 ± 0.1 eV, a vacancy formation enthalpy of 3.67 ± 0.2 eV, and an entropy factor of $2.3\,k_{\mathrm{B}}$. These values are in good agreement with Doppler-broadening data on vacancies in thermal equilibrium [17, 18].

Vacancy-cluster formation and coarsening are reported at the same temperature independently of which mechanism of irradiation damage is operative (alpha-irradiated [19] or electron-irradiated [15] samples). In the literature, vacancy loops (=dislocation loops) are cited, with a positron lifetime of about 150 ps [10]. This is in good accordance with the positron lifetime in dislocations determined in our study: $\tau_{\mathrm{disl}} = 153 \pm 2$ ps.

3.2.3. Sintering of powder compacts. Positrons in powders, or porous materials in general, are assumed to thermalize only within a powder-particle or compact region, and then start diffusing (see part I [6] and [1]). In this way, they possibly reach interfaces and surfaces. We can assume that all information obtained by POLIS is concerned with the inside of the powder particles. If we detect a surface component, positrons certainly reach the contact boundaries too. Assuming that the pore surface is of the same order of magnitude as the contact boundary area, it should be clear that a comparable fraction of positrons will reach the contact boundaries as well, and, hence, an even larger fraction will annihilate in the contact boundary zone (see the discussion in part I [6] and in [1]).

In the analysis of the lifetime data, we proceeded as follows: for the two smallest powder-particle sizes, i.e. 0.4 and 1.8 μm, we performed, over the temperature range from 20 to

Table 3. Averages for the positron lifetimes in defects detected, using a three-component free decomposition over the temperature range 20 °C to 900 °C. It is plausible to assume nearly complete trapping of positrons into defects.

	0.4 μm	1.8 μm	Type of defect
$\bar{\tau}_2$ (ps)	152 ± 5	151 ± 5	Dislocations/small-angle GBs
$\bar{\tau}_3$ (ps)	324 ± 30	307 ± 30	Vacancy clusters/large-angle GBs
$\bar{\tau}_4$ (ps)	610 ± 40	616 ± 40	Surface states

900 °C, a three-component free decomposition, leading to the average lifetimes for the three fitted components given in table 3 (due to the quite large errors in fitting the longest lifetime, there was quite a lot of scatter in the decomposition).

So we can attribute the three observed lifetime components to (i) dislocations or small-angle grain boundaries, (ii) vacancy clusters or large-angle grain boundaries, and (iii) annihilation in surface states. Since we can assume that positrons trapped at each surface state have a definite defect-related lifetime, fixing the surface lifetime at 615 ps is justified, because this was the average value obtained from free fits. Fixing τ_{surf} is necessary to stabilize the decomposition of the spectra. See figure 4 for the shrinkage velocity and for the change of the average positron lifetime, and figures 5, 6, and 7 for the change of the intensities corresponding to the different defect-related positron lifetimes in compacts of tungsten powder with different powder-particle sizes.

There are, at least, three different types of defect present. Even for the uncompressed powder we find—especially for smaller powder-particle sizes—a dislocation signal (151 ps; this could be arising from dislocations or small-angle grain boundaries, and possibly also monovacancies), a vacancy-cluster-like signal (300 ps; this could be arising from vacancy clusters in the volume or large-angle grain boundaries), and a positron lifetime at surfaces ($\approx$615 ps). But this is not the case for the largest powder-particle size (75 μm), in which case the positron lifetime is a single-component one, and is nearly that of the perfect lattice (107 instead of 103 ps), and for the next-smaller powder-particle size (23 μm), in which case the lifetime analysis showed $\tau_1 \approx \tau_{\mathrm{b}}$ and $\tau_2 \approx 285$ ps with only a few per cent intensity (see table 4). This again shows that positrons can thermalize only within the powder particles, since there was no noticeable lifetime component reflecting annihilation in the air between the powder particles.

After pressing, the average lifetime decreases for the compacts with smaller powder-particle sizes but increases for compacts with larger powder-particle sizes (see figure 4(b)). We attributed this to a decreasing signal from the surface state (615 ps) on the one hand and an increasing signal from dislocations or small-angle grain boundaries on the other hand (see figures 6 and 7). The intensity corresponding to the surface lifetime decreases upon pressing for all powder-particle sizes, due to reduction of the surface area (see figure 6). The increasing dislocation signal is apparently due to the generation of dislocations and/or the formation of small-angle grain boundaries by means of plastic deformation during pressing (see figure 7).

The vacancy/dislocation-like signal can only partly be due to monovacancies, since otherwise this lifetime component would vanish above 400 °C, where vacancies become mobile (see the discussion in section 3.2.2). Due to the small difference between $\tau_{\mathrm{disl}} \approx 153$ ps and $\tau_{\mathrm{b}} \approx 103$ ps, these lifetimes cannot be resolved [5]. For compacts of 0.4 μm powder, the drop in the average lifetime coincides with the onset of the shrinkage. See figure 4.

Because of the different reduction temperature of tungsten oxide, it is not surprising that we measure for the smaller powders increasing signals from large-angle grain boundaries, i.e. I_3 corresponding to $\tau_{\mathrm{GB}} \approx 315$ ps, and dislocations/small-angle grain boundaries, i.e. I_2

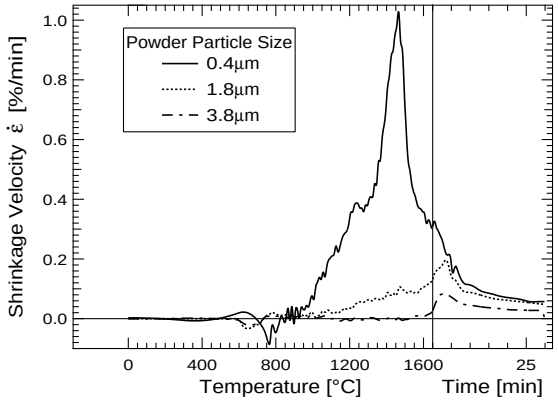

(a)

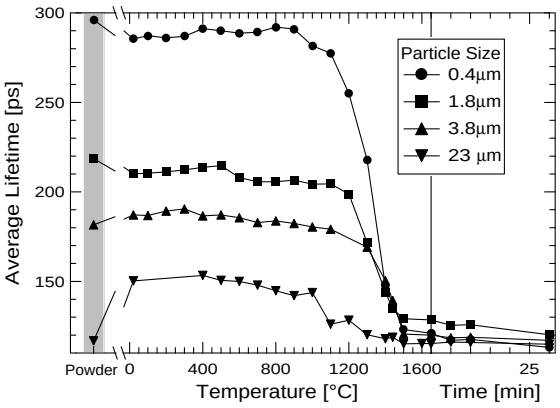

(b)

Figure 4. Compacts of tungsten powder with different powder-particle sizes; the compaction pressure was 700 MPa in each case. The shrinkage rates are given in (a). Only compacts of 0.4 μm powder show a pronounced maximum of the shrinkage rate during heating. For larger powder-particle sizes the maximum is reached in the isothermal sintering stage. 23 μm powder did not show any significant shrinkage, and hence the results for this powder are not plotted. (b) shows the average lifetime. Note the very similar annealing behaviours for all powder-particle sizes, except perhaps the largest powder-particle size.

corresponding to $\tau_{\mathrm{disl}} \approx 153$ ps (see figures 5 and 7, and the discussion in section 2).

Due to deformation caused by pressing, there seems to be (at least in the case of larger powder particles) dislocation glide and dislocation intersection, and hence monovacancies can be generated via jog dragging [20] (see figure 7). Subsequently, vacancies are likely to form agglomerates or just remain in the matrix, since monovacancies in tungsten are known to become mobile only above 400 °C. On pressing the sample with the smallest powder-particle size, the defect structure detected by POLIS does not change significantly, except that the intensity of the surface state is decreased for the pressed compact (see figure 6).

Since the 23 μm powder was nearly free of defects before the pressing (see table 4), we can assume from the annealing curve for compacts of 23 μm powder that we see coarsening of vacancy clusters indicated by the increase of the corresponding lifetime. Above 1100 °C, the clus-

Table 4. Three-component decompositions for uncompacted powder and pressed compacts in comparison; the pressure applied was 700 MPa in all cases. All of the spectra were obtained from at least 6×10^6 counts except that for the 3.8 μm compact. Positron lifetimes in dislocations and in the bulk are not resolved. They are subsumed in τ_2.

	$\bar{\tau}$ (ps)	χ^2	τ_2 (ps) I_2 (%)	τ_3 (ps) I_3 (%)	τ_4 (ps) I_4 (%)
0.4 μm powder	297.3	0.967	151 ± 3 31.4 ± 1.2	337 ± 4 64.0 ± 0.9	751 ± 22 4.5 ± 0.5
0.4 μm compact	284.8	1.103	142 ± 6 28.1 ± 2.8	300 ± 10 59.9 ± 1.4	543 ± 20 12.0 ± 2.2
1.8 μm powder	217.0	1.005	110 ± 74 40.1 ± 5.7	234 ± 164 46.9 ± 3.9	482 ± 20 13.1 ± 2.3
1.8 μm compact	209.9	1.048	151 ± 3 65.8 ± 3.2	290 ± 16 30.1 ± 2.2	571 ± 39 4.2 ± 1.3
3.8 μm powder	180.6	0.935	102 ± 5 53.1 ± 4.3	227 ± 13 40.2 ± 3.3	522 ± 27 6.7 ± 1.3
3.8 μm compact	186.7	0.998	144 ± 11 65.0 ± 18.8	236 ± 48 30.8 ± 16.3	488 ± 72 4.3 ± 2.8
23 μm powder	116.8	1.071	113 ± 1 98.0 ± 0.3	285 ± 12 2.0 ± 0.3	
23 μm compact	150.3	0.998	134 ± 1 88.6 ± 0.6	279 ± 4 11.4 ± 0.6	
75 μm powder	106.9	1.007	107 ± 1 100		

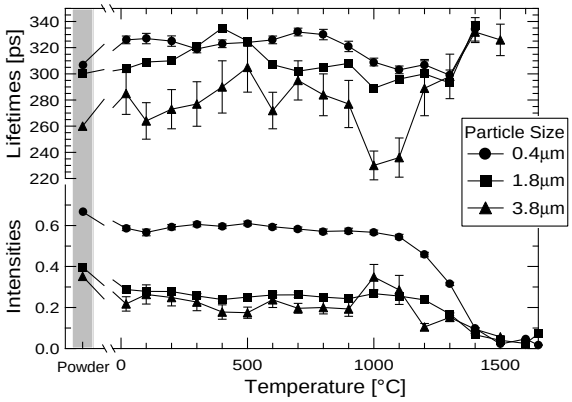

Figure 5. Compacts of tungsten powder (700 MPa); the graph shows the positron lifetime in vacancy clusters or large-angle grain boundaries, and the corresponding intensity for compacts of tungsten powder with different powder-particle sizes. We see that the positron lifetime is nearly constant at around 300 ps, while the corresponding intensities show a distinct annealing step between 1200 and 1400 °C. Below 1000 °C, the lifetime of 300 ps could have a mixed origin, i.e. it could reflect positron trapping at clusters and at grain boundaries.

ters seem to have dissolved, since the corresponding intensity goes to zero. A multi-component decomposition of the spectra is omitted, since this powder is irrelevant to the sintering mecha-

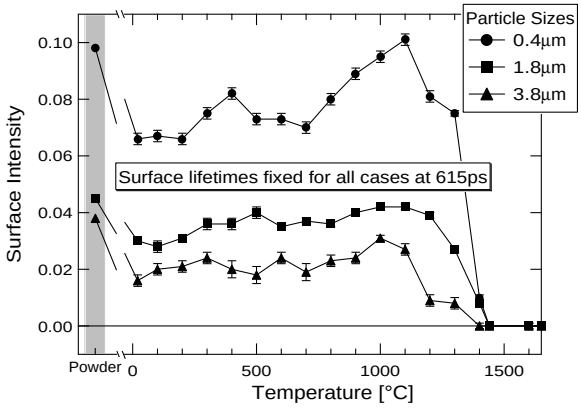

Figure 6. Compacts of tungsten powder (700 MPa); the figure gives the surface intensity for compacts of tungsten powder with different powder-particle sizes. The corresponding lifetime for positrons trapped in surface states was fixed at 615 ps. We see that the intensities are nearly constant until they tend to zero between 1200 and 1400 °C. Note that the intensity decreases from the uncompacted to the compacted state due to destruction of free surface area.

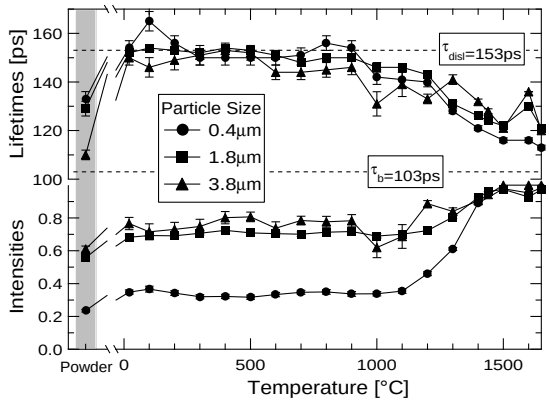

Figure 7. The change in the first lifetime component that occurs during heat treatment for powder compacts with different powder-particle sizes. In the powder and above 1100 °C, τ_2 reflects both the annihilation of positrons trapped at dislocations ($\tau_2 \approx 153$ ps) and annihilation in the undisturbed volume ($\tau_2 \approx 103$ ps). Since these components are not separable, it could reflect any combination of them.

nisms. Between 1200 and 1400 °C, there is another annealing stage, probably due to the annealing out of dislocations (see figure 4). But the positron lifetime in dislocations could not be resolved from the bulk lifetime, since the difference was less than 50 ps [5]. At 1400 °C, compacts with this powder-particle size again show nearly the same defect structure as before the pressing.

Alternatively to the three-component decomposition otherwise used throughout this article, in some cases a four-component decomposition of the lifetime spectra is possible—at least for the uncompacted powders (23 μm and 75 μm powders lead to only two- and one-component spectra, respectively).

From table 5 we can estimate defect densities for the uncompacted powders (in as-produced form). They will be given in section 3.3 in comparison with x-ray diffraction data.

Table 5. Four-component decompositions for uncompacted and compacted powders. The pressure applied was 700 MPa in all cases. All spectra were obtained from at least 6×10^6 counts. The data show that a meaningful four-component decomposition is possible.

	$\bar{\tau}$	χ^2	τ_1^{calc} (ps)	τ_1 (ps) I_1 (%)	τ_2 (ps) I_2 (%)	τ_3 (ps) I_3 (%)	τ_4 (ps) I_4 (%)
0.4 μm	292.9	0.922	4 ± 10	40 ± 36	156 ± 10	327 ± 14	615 fix
powder				2.0 ± 0.9	29.4 ± 1.4	61.0 ± 1.8	7.6 ± 0.2
0.4 μm	283.7	1.106	4 ± 10	23 ± 18	151 fix	321 ± 2	615 fix
compact				1.0 ± 0.8	32.1 ± 1.0	59.9 ± 0.3	7.0 ± 0.2
1.8 μm	214.4	0.991	21 ± 15	56 ± 28	155 ± 14	335 ± 19	615 fix
powder				10.5 ± 5.4	56.4 ± 2.7	29.5 ± 4.3	3.6 ± 0.5
3.8 μm	179.9	0.931	48 ± 20	82 ± 20	151 fix	298 ± 15	615 fix
powder				28.3 ± 5.5	45.9 ± 8.4	22.5 ± 2.8	3.3 ± 0.3

3.3. Grain sizes obtained by x-ray line-profile analysis

The evaluation of the line broadening of x-ray diffraction peaks can reveal information about lattice disorder of the second kind, such as dislocations, twins, and small- and large-angle grain boundaries (if <0.5 μm). The condition that crystallites should be statistically equal as regards their microstructure is fulfilled for the materials considered here, since they each consist of very fine powders of micron and submicron sizes. The observable line shape of the x-ray diffraction peak $F(x)$ is always a convolution of a line profile $g(u)$ (the instrumental resolution), due to the non-ideal conditions of the scattering experiment, and a physical line profile $f(x)$, due to the lattice disorder. This gives

$$F(x) = \int g(u) f(x-u)\, \mathrm{d}u \tag{1}$$

where the function $g(u)$ is determined with the help of a reference sample. Then, $g(u)$ and $f(x)$ can be deconvoluted by a Fourier transformation using the Stokes correction [21].

3.3.1. Fourier analysis. There are theoretical considerations indicating that the line shape $f(x)$ is a convolution of partial profiles which are related to the statistically independent components of the lattice disorder. Hence, for the evaluation of the physical line broadening, we can make an *ansatz* for the Fourier coefficients as a product:

$$A(L) = a_{\text{p}}(L) a_{\epsilon}(L) a_{\text{d}}(L) \tag{2}$$

where $a_{\text{p}}(L)$ is due to particle-size effects, $a_{\epsilon}(L)$ due to strain effects, and $a_{\text{d}}(L)$ due to dislocations.

Using the results of the kinematic theory of x-ray scattering by imperfect crystalline solids [22–24], one obtains for the Fourier coefficients $A(L)$ of the physical line profile

$$A(L) \approx \exp(-L/D) \exp(-K \langle \epsilon^2 \rangle L^2) \exp(-B \ln(L_0/L) L^2) \tag{3}$$

and

$$-\ln A(L) = L/D + \left[K \langle \epsilon^2 \rangle + B \ln(L_0/L) \right] L^2 \tag{4}$$

where $L = n d_{hkl}$ is the measuring length perpendicular to the scattering lattice planes (hkl), $D = D(hkl)$ is the x-ray domain size (effective particle size), $B = B(hkl)$ is a factor proportional to the mean total dislocation density†, L_0 is a length proportional to the cut-off radius

† This includes dislocations randomly distributed inside subgrains as well as dislocations in low-angle grain boundaries.

R_c of the strain field of dislocations, and $\langle\epsilon^2\rangle = \langle\epsilon^2(hkl)\rangle$ is the mean square microstrain due to internal stress of the second kind.

3.3.2. Warren–Averbach analysis. Using the assumptions of the traditional Warren–Averbach analysis [22,25–27] and following the derivation in [28], equation (4) leads to the function

$$\Phi(L) = -\ln A(L)/L = 1/D + K\langle e^2(L)\rangle L \tag{5}$$

where $K = 2\pi^2(h^2 + k^2 + l^2)/a_0$ (a_0 is the lattice parameter). The graph of this function has been called a *Warren–Averbach plot* [29, 30]. The constant part $\Phi(0) = 1/D$ of $\Phi(L)$ allows the determination of an apparent reciprocal x-ray domain size, while the linear part gives an *effective* mean square strain via $(\mathrm{d}\Phi/\mathrm{d}L)_{L\to 0} = K\langle e^2(hkl)\rangle$. As regards to concrete lattice defects, the interpretation of the quantities requires additional information. The x-ray domain size D, for instance, is determined by small grain sizes (<0.5 μm), subgrain sizes, and whether there are twins and stacking faults present; furthermore, D can be influenced by structural inhomogeneities as well. The data are reliable only if the x-ray domain size is significantly smaller than 0.5 μm.

3.3.3. Krivoglaz–Wilkens analysis. Using the model of a restricted random distribution of dislocations introduced by Krivoglaz [24, 31, 32] and Wilkens [23, 33], one obtains from (3)

$$\Psi(L) = -\ln A(L)/L^2 = 1/DL + (K\langle\epsilon^2(L)\rangle + B\ln L_0) - B\ln L. \tag{6}$$

The graph of this function is called a *Krivoglaz–Wilkens plot* [28–30]. At higher L it has a linear branch. Its slope gives $B(hkl)$ and, hence, a quantity proportional to the dislocation density via

$$\mathrm{d}\Psi/\mathrm{d}(\ln L)_{L\gg 1} = B \sim N_{\mathrm{disl}} \qquad (K\langle\epsilon^2\rangle + B\ln L_0) - B\ln L = 0. \tag{7}$$

For further details, see [28, 29, 34].

3.3.4. Experimental results. As experimental results, we obtain the x-ray domain sizes D and the dislocation densities N_{disl} given in tables 6, 7, and 8. The results are discussed in section 4.

Table 6. X-ray domain sizes D and dislocation densities N_{disl} estimated from x-ray line-profile analysis, as well as the dislocation densities N_{disl}, and powder-particle ($\bar{L}_P$) and grain sizes ($\bar{L}_G$) estimated from positron annihilation data for uncompacted tungsten powders with different average powder-particle sizes $\bar{L}_P^{\mathrm{sup}}$ as given by the supplier.

	X-ray diffraction		POLIS		
$\bar{L}_P^{\mathrm{sup}}$ (μm)	D (μm)	N_{disl} (10^{11} cm^{-2})	$\bar{L}_P$ (μm)	$\bar{L}_G$ (μm)	N_{disl} (10^{11} cm^{-2})
0.4	0.08 ± 0.04	2.5 ± 0.3	0.5 ± 0.2	$\leqslant 0.1$	1.0 ± 0.8
1.8	0.15 ± 0.07	0.58 ± 0.09	2.5 ± 1.0	0.3 ± 0.15	0.29 ± 0.1
3.8	> 0.5	0.25 ± 0.05	4.0 ± 1.0	1.1 ± 0.3	0.066 ± 0.02
23	$\gg 0.5$	< 0.05	$\gg 15$	8.0 ± 3.0	< 0.005

4. Discussion

This section contains a discussion of the results given in section 3. We will consider the data obtained on the sintering process in the light of the results on the annealing kinetics of plastically deformed and electron-irradiated samples.

Table 7. X-ray domain sizes D and dislocation densities N_{disl} estimated from x-ray line-profile analysis, as well as grain sizes $\bar{L}_{\mathrm{G}}$ estimated from metallography (SEM) and positron annihilation data (and additionally the dislocation densities N_{disl}) for compacts with an average powder-particle size of $\bar{L}_{\mathrm{P}}^{\mathrm{sup}} = 0.4\ \mu$m. The domain size indicated for 1300 and 1400 °C could be an artifact.

	X-ray diffraction		Metallography	POLIS	
T (°C)	D (μm)	N_{disl} (10^{11} cm^{-2})	$\bar{L}_{\mathrm{G}}$ (μm)	$\bar{L}_{\mathrm{G}}$ (μm)	N_{disl} (10^{11} cm^{-2})
100	0.053 ± 0.03	3.3 ± 0.4	≈ 0.1	$\leqslant 0.1$	2.6 ± 2.0
600	0.063 ± 0.03	2.9 ± 0.4	≈ 0.1	$\leqslant 0.1$	2.5 ± 2.0
1200	—	—	—	0.28 ± 0.1	0.22 ± 0.1
1300	0.25 ± 0.2	0.18 ± 0.04	≈ 0.6	0.8 ± 0.3	0.07 ± 0.05
1400	0.25 ± 0.2	< 0.05	≈ 2.0	2.5 ± 0.7	< 0.005
1650	$\gg 0.5$	< 0.05	≈ 8	8.0 ± 3.0	< 0.002

Table 8. X-ray domain sizes D and dislocation densities N_{disl} estimated from x-ray line-profile analysis, as well as grain sizes $\bar{L}_{\mathrm{G}}$ estimated from metallography (SEM) and positron annihilation data (this additionally gives the dislocation densities N_{disl}) for compacts with an average powder-particle size of $\bar{L}_{\mathrm{P}}^{\mathrm{sup}} = 1.8\ \mu$m.

	X-ray diffraction		Metallography	POLIS	
T (°C)	D (μm)	N_{disl} (10^{11} cm^{-2})	$\bar{L}_{\mathrm{G}}$ (μm)	$\bar{L}_{\mathrm{G}}$ (μm)	N_{disl} (10^{11} cm^{-2})
100	0.2 ± 0.1	1.87 ± 0.28	≈ 0.5	0.13 ± 0.08	2.0 ± 1.3
600	0.17 ± 0.1	1.43 ± 0.21	≈ 0.8	0.15 ± 0.08	2.0 ± 1.3
1200	—	—	—	0.4 ± 0.2	0.82 ± 0.3
1300	> 0.5	0.48 ± 0.11	≈ 1.1	2.0 ± 1.0	0.2 ± 0.15
1400	$\gg 0.5$	0.13 ± 0.03	≈ 2.0	3.3 ± 1.5	0.04 ± 0.025
1650	$\gg 0.5$	< 0.05	≈ 6.0	6.0 ± 3.0	< 0.003

4.1. Compaction

Pressing the powder, apparently, generates defects (leading to increasing intensity of the dislocation/small-angle grain boundary signals) as a result of the plastic deformation of powder particles. It is also known from fatigue experiments that the movement of jogged dislocations creates vacancies. The jog-generated vacancies are closely associated with the dislocation jog which generated them [20]. They have a tendency to cluster [35, 36]. This can be seen from a comparison of the uncompressed state with the compacted powder (see table 4 and figure 7). But with decreasing powder-particle size, the as-produced state of the powder contains an increasing density of lattice defects. And hence the smaller the powder-particle size becomes, the more difficult it is to work out the influence of the pressing.

4.2. Electron irradiation and quenching

Results on the annealing kinetics (i) after electron irradiation obtained by means of POLIS [15] and (ii) after quenching obtained by means of electrical resistometry [16] indicate that mono-vacancies become mobile slightly below 400 °C (670 K). At this temperature these mono-vacancies form vacancy clusters, which then coarsen above 450 °C, and finally anneal out totally at about 1100 °C (1370 K) [15]. TEM investigations after quenching and partial recovery revealed the presence of microvoids [16].

4.3. Plastic deformation

Investigation of the as-deformed state of a tungsten sheet, in as-produced (hot-rolled) form, reveals as defects monovacancies, dislocations, and vacancy clusters. A drop of τ_2 from 165 ps to 153 ps at 400 °C is observed, since monovacancies become mobile at that temperature, and hence $\tau_2 = 153$ ps must reflect trapping of positrons at dislocations. Below 400 °C, the second lifetime relates to a combination of a monovacancy signal and a dislocation signal. This assertion is supported by $\tau_2 = 153 \pm 2$ ps remaining constant above 500 °C. Above 400 °C, a coarsening of previously existing vacancy clusters is observed. During subsequent annealing at higher temperatures, further coarsening of the clusters is observed. The clusters finally anneal out totally at about 1000 °C, which is nearly the same as the temperature after electron irradiation. For temperatures higher than 1000 °C, it is exclusively the dislocation signal that remains, while the dislocation density decreases further. Even though, in the literature, 1200–1300 °C (0.4 T_M) is given as the recrystallization temperature for heavily deformed high-purity tungsten [13, 14], we fail to observe this annealing stage. Hence we have to suspect that either the purity of our sample was not sufficient or the degree of deformation was too low.

4.4. Determination of the grain and powder-particle sizes

The method of determination of x-ray domain sizes has been explained in section 3.3. The grain sizes estimated from positron lifetime data are determined by assuming complete positron capture at grain boundaries if they are reached during the diffusive motion. As described in part I [6] and in [1], we can then estimate the fraction of positrons reaching the boundaries via the trapping model. Assuming that the POLIS signal with a lifetime of about 300 ps exclusively stems from grain boundaries, we can estimate by comparison to the Monte Carlo simulation results [37] the average grain sizes $\bar{L}_G$. This is justified at least for temperatures higher than 1000 °C, since, as we have seen in sections 3.2.1 and 3.2.2, vacancy clusters are not likely to exist at such high temperatures. But even for lower temperatures, the deviation due to eventually existing vacancy clusters will be small, since we did not observe an annealing stage of the corresponding lifetime component. Furthermore, since positrons can be trapped by defects on their diffusion path into large-angle grain boundaries, we have taken into account the trapping of positrons by dislocations (in the volume or in subboundaries) from the estimates presented in [37].

The dislocation density is estimated from the positron data as follows. To obtain N_{disl} we use the simple trapping model, i.e. assuming that the dislocations are randomly distributed. Since to our knowledge no trapping coefficient (relating the trapping rate to the dislocation density) is given in the literature, we take the known values for copper, nickel, and iron: $\mu_{disl} = 1.0 \pm 0.2$ cm^2 s^{-1}. The errors given for the dislocation densities are related to the methods used. They could include systematic scaling errors.

We cannot give an estimate of the subgrain size from the POLIS data, since we cannot definitely distinguish between dislocations randomly distributed in the volume and those arranged in walls (subgrains).

For the uncompacted powders, we obtained the data given in table 6. We see that the measured x-ray domain sizes are always smaller than the powder-particle sizes. In table 6, grain sizes and dislocation densities estimated from the positron data are given as well.

For the pressed and sintered samples, the results given in tables 7 and 8 show the x-ray domain sizes and grain sizes increasing with temperature detected using different methods (1650 °C corresponds to the sample held at this temperature for 10 min). The grain sizes determined from metallography are only rough estimates (within a factor of 2) because of

the poor statistics. The data show that with increasing temperature we see recovery and recrystallization processes, indicated by decreasing dislocation densities and/or increasing subgrain sizes, at around 1300 °C. This process is accompanied by grain growth; see table 9 for the defect-related positron lifetimes determined.

Table 9. Positron data for tungsten, according to our results.

Lifetime in	
Bulk	$\tau_b = 103 \pm 2$ ps
Dislocations	$\tau_{disl} = 153 \pm 2$ ps
Vacancies	$\tau_v > 165$ ps
Grain boundaries	$\tau_{GB} = 315 \pm 30$ ps
Surface	$\tau_{surf} = 615 \pm 40$ ps

Table 10. Grain sizes $\bar{L}_G$ and dislocation densities N_{disl} (10^{11} cm^{-2}) estimated from positron annihilation data for compacts with a powder-particle size of 3.8 μm.

T (°C)	$\bar{L}_G$ (μm)	N_{disl} (10^{11} cm^{-2})
100	0.4 ± 0.2	2.0 ± 1.5
600	0.6 ± 0.2	1.0 ± 0.7
1200	0.8 ± 0.3	0.7 ± 0.2
1300	1.3 ± 0.5	0.5 ± 0.2
1400	1.9 ± 0.5	0.007 ± 0.004
1650	> 8	< 0.005

For comparison, we give in table 10 the corresponding POLIS data for $\bar{L}_P = 3.8$ μm as well, even though the samples did not show any significant shrinkage.

4.5. Sintering

By choosing different powder-particle sizes, we varied the driving force for sintering over a wide range. This can be seen clearly from the experimental shrinkage curves (see figure 4(a)); only the samples with the two smallest particle sizes showed significant shrinkage. From the lifetime results, we can conclude that the smaller the powder-particle size, the greater the number of positron traps existing inside the powder particles in the as-produced state. Making a comparison to the results on electron-irradiated and plastically deformed samples, we can conclude from the annealing kinetics of the compacts that large- and small-angle grain boundaries must play a dominant role in positron trapping (besides the trapping at surfaces).

The small sizes of the grains inside the powder particles of the two smallest sizes are sufficient to explain the positron lifetime spectra when considering the observed large-angle grain boundaries as the predominant positron traps—leading to vacancy-cluster-like signals with lifetimes of about 300 ps (see section 3.2). If we assume dislocations or small-angle grain boundaries inside these grains, the lifetime signals become understandable. At 1200, 1300, and 1400 °C, the vacancy-cluster-like lifetimes for the three smallest powder-particle sizes are nearly equal (see figure 5). Since in that temperature range, according to irradiation and deformation experiments, vacancy clusters have already annealed out, this indicates that we are detecting the same type of defect—large-angle grain boundaries.

Independently of their powder-particle sizes, all of the samples show similar annealing behaviours, but the relative intensities differ due to the different sizes of the grains inside the powder particles. Between 1200 and 1400 °C, recrystallization and grain growth is observed

(see figures 4, 5, and 6 as well as tables 7, 8, and 10), while the vanishing of the surface component at that temperature indicates annihilation of pore surface, and hence shrinkage.

So, we are monitoring, by means of positron lifetime spectroscopy, the recovery and recrystallization, as well as the change in the inner surfaces, i.e. the smoothing of the pore shape and the vanishing of pore space.

4.6. Possible shrinkage mechanisms

Diffusional creep has been discussed in part I, where the corresponding equations were given—i.e. Nabarro–Herring creep, Coble creep, and dislocation creep. According to figure 7, the possibility of dislocation creep can be excluded at least for temperatures above 1400 °C on the basis of the same argument as is given in part I. The two-particle model uses the equations given in part I.

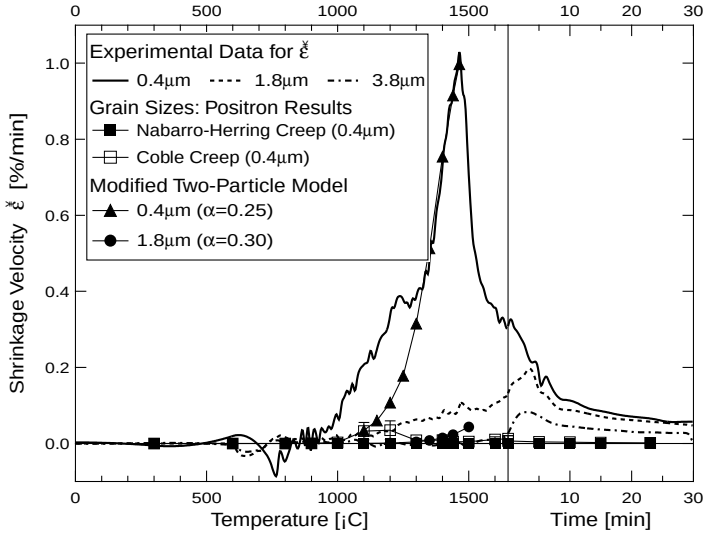

Figure 8. Compacts of tungsten powder with different powder-particle sizes sintered at a heating rate of 30 K min^{-1}; the shrinkage rates for different mechanisms are estimated from experimental results. One can see a good coincidence for the modified two-particle model. The model loses validity when grain growth starts (1400–1500 °C).

The shrinkage rates in figure 8 are estimated for diffusional creep according to the lifetime data. This gives $\bar{L}_{\mathrm{P}}$ and $\bar{L}_{\mathrm{G}}$, while the experimentally determined shrinkage and $\bar{L}_{\mathrm{P}}$ are used in the two-particle model (see [38–40] and the discussion in part I). We calculate from the lifetime data, by using the trapping model, the fraction of positrons reaching surfaces and interfaces. Together with the Monte Carlo results on the positron diffusion [37], this gives the effective grain ($\bar{L}_{\mathrm{G}}$) and powder-particle sizes ($\bar{L}_{\mathrm{P}}$). Throughout the calculation of the shrinkage rates, the powder-particle sizes are fixed at $\bar{L}_{\mathrm{P}} = 0.4\ \mu$m, $\bar{L}_{\mathrm{P}} = 1.8\ \mu$m, and $\bar{L}_{\mathrm{P}} = 3.8\ \mu$m. Below, the relevant constants used in the calculations are given. They have been taken from [41]: the Boltzmann constant $k_{\mathrm{B}} = 8.617 \times 10^{-5}$ eV K^{-1}; the volume diffusion coefficient $D_{\mathrm{vol}} = D_0^{\mathrm{vol}} \exp(-Q_{\mathrm{vol}}/k_{\mathrm{B}}T)$ ($D_0^{\mathrm{vol}} = 5.6 \times 10^{-4}$ $\mathrm{m}^2\ \mathrm{s}^{-1}$, $Q_{\mathrm{vol}} = 6.07$ eV); the grain boundary diffusion coefficient $D_{\mathrm{GB}} = D_0^{\mathrm{GB}} \exp(-Q_{\mathrm{GB}}/k_{\mathrm{B}}T)$ ($D_0^{\mathrm{GB}} = 10.0 \times 10^{-4}$ $\mathrm{m}^2\ \mathrm{s}^{-1}$, $Q_{\mathrm{GB}} = 3.99$ eV); the surface tension $\gamma_{\mathrm{S}} = 3.323$ J m^{-2}; the grain boundary tension $\gamma_{\mathrm{GB}} = 1.080$ J m^{-2}; the atomic volume $\Omega = 1.59 \times 10^{-29}$ m^3; and the effective cross section of grain boundary diffusion $\delta_{\mathrm{GB}} = 5.41 \times 10^{-10}$m; while the geometric

constants $A_0 = 1, \ldots, 4$, $A_1 \approx 10$, $A_2 \approx 150$ are taken from [7]. The porosity Θ is calculated from shrinkage data.

In figure 8 we compare the shrinkage rates obtained by dilatometric measurement to the calculated ones. Since equations (2)–(4) in part I describing creep in porous bodies underestimate the sharp curvature gradient in the initial stage, we considered the modified two-particle model (described in part I—equations (6) and (7)), additionally taking into account the flattening of powder particles caused by pressing. We can see from figure 8 that the modified two-particle model leads to reasonable shrinkage rates, at least for the smallest powder-particle size. Over the whole temperature range considered, the shrinkage rate according to Nabarro–Herring creep is at least some orders of magnitude smaller than that according to the Coble creep.

5. Conclusions

From metallography, x-ray diffraction, and POLIS investigations, we can conclude that powder particles, especially smaller ones, possess inner microstructure; i.e. there are large- and small-angle grain boundaries and/or dislocations and vacancy clusters, possibly due to the production process.

Vacancy clusters in the volume, as observed after electron irradiation or plastic deformation by means of POLIS, anneal out at much lower temperature compared to the cluster-like signals in the pressed and sintered samples. Hence, the cluster signal is interpreted as indicating positron annihilation at large-angle grain boundaries. The grain size can be estimated from POLIS data together with the results from the Monte Carlo simulation of positron diffusion. The interpretation of the positron trapping and annihilation at grain boundaries is in good agreement with the grain sizes estimated from metallography and x-ray diffraction. Hence we are, essentially, detecting, by means of POLIS, recovery, recrystallization, and grain growth. This assertion is supported by the fact that—independently of the different sintering behaviours—the annealing curves for all of the powder-particle sizes are very similar. They differ mainly in the intensity corresponding to annihilation at surfaces and at grain boundaries. But the annealing stages themselves are observed at the same temperatures.

The shrinkage rate differs according to the powder-particle size, i.e. depending on the driving force; significant shrinkage is observed only for the smallest two powder-particle sizes, since the sintering temperature of $0.52\ T_M$ was two low when the driving force (proportional to the inverse powder-particle size) was reduced. By considering shrinkage rates calculated according to a modified two-particle model, which takes into account the flattening of powder particles due to pressing, we derive values which are reasonable until massive grain growth occurs and the assumptions of the model break down. The main contribution to the material transport stems from grain boundary diffusion. Hence, Coble creep seems to be the dominant process of material transport during the sintering of tungsten at the temperature of 1650 °C ($0.52\ T_M$), while the role of volume diffusion can be neglected due to the comparatively low sintering temperature.

Acknowledgments

We would like to thank Professor W Schatt and Dr K-P Wieters (both at TU Dresden) for many interesting discussions, W Zeiger (TU Dresden) for the preparation of the sintered samples (part of his diploma thesis work), Dr F Dworschak (KFA Jülich) for preparing the electron-irradiated samples, A Mensch and G Trommer (both at TU Dresden) for the fine SEM pictures, and Dr Hase and Dr C Blank for their support during the metallographic preparation at the TU Dresden.

References

[1] Staab T E M, Krause-Rehberg R and Kieback B 1999 Positron annihilation in fine-grained materials and fine powders—an application to sintering of technically used metal powders *J. Mater. Sci.* at press

[2] Schaefer H E 1987 Investigation of thermal equilibrium vacancies in metals by positron annihilation *Phys. Status Solidi* a **102** 47–65

[3] Schultz P J and Lynn K G 1988 Interaction of positron beams with surfaces, thin films and interfaces *Rev. Mod. Phys.* **60** 701–79

[4] Puska M J and Nieminen R M 1994 Theory of positrons in solids and on solid surfaces *Rev. Mod. Phys.* **66** 841–97

[5] Somieski B, Staab T E M and Krause-Rehberg R 1996 The data treatment influence on the spectra decomposition in positron lifetime spectroscopy; part 1: On the interpretation of multi-component analysis studied by Monte Carlo simulated model spectra *Nucl. Instrum. Methods* A **381** 128–40

[6] Staab T E M, Krause-Rehberg R, Vetter B and Kieback B 1999 The influence of microstructure on the sintering process in crystalline metal powders investigated by positron lifetime spectroscopy: I. Electrolytic and spherical copper powders *J. Phys.: Condens. Matter* **11** 1757

[7] Schatt W 1992 *Sintervorgänge* 1st edn (Düsseldorf: VDI)

[8] Geguzin Ja E 1973 *Physik des Sinterns* 1st edn (Leipzig: VEB Deutscher Verlag für Grundstoffindustrie)

[9] Hübner C G, Staab T and Leipner H S 1995 TEM studies of the microstructure of pressureless sintered copper *Phys. Status Solidi* a **150** 653–60

[10] de Vries J 1987 *PhD Thesis* University of Delft

[11] Vehanen A, Lynn K G, Schultz P J, Cartier E, Güntherodt H-H and Parkin D M 1984 *Phys. Rev.* B **29** 2371

[12] Soininen E, Huomo H, Huttunen P A, Mäkinen J, Vehanen A and Hautojärvi P 1990 Temperature dependence of positron diffusion in cubic metals *Phys. Rev.* B **41** 6227–33

[13] Schultz H 1959 Untersuchungen über Gitterfehlstellen in kaltverformtem Wolfram mit Hilfe von Restwiderstandsmessungen *Z. Naturf.* a **14** 361–73

[14] Schultz H 1964 Die Erholung des elektrischen Widerstandes von kaltverformtem Wolfram *Acta Metall.* **12** 649–64

[15] Schaefer H E, Valenta P, Saile B and Maier K 1979 Positron annihilation in electron irradiated refractory metals *Proc. 5th Conf. on Positron Annihilation* ed R R Hasiguti and K Fujiwara (Sendai: The Japan Institute of Metals) pp 747–50

[16] Rasch K-D, Siegel R W and Schultz H 1980 Quenching and recovery investigations of vacancies in tungsten *Phil. Mag.* A **41** 91–117

[17] Maier K, Peo M, Saile B, Schaefer H-E and Seeger A 1979 High-temperature positron annihilation and vacancy formation in refractory metals *Phil. Mag.* A **40** 701–28

[18] Maier K 1983 Defects in thermal equilibrium: positron annihilation and other methods *Proc. Int. 'Enrico Fermi' School of Physics on Positron Solid State Physics* ed W Brandt and A Dupasquier (Amsterdam: North-Holland) pp 265–97

[19] Nambissan P M G and Sen P 1992 Positron annihilation studies of the annealing behaviour of alpha irradiated tungsten *Radiat. Eff.* **124** 215–21

[20] Hull D and Bacon D J 1984 *Introduction to Dislocations* 3rd edn (Oxford: Pergamon)

[21] Stokes A R 1948 A numerical Fourier-analysis method for the correction of widths and shapes of lines on x-ray powder photographs *Proc. Phys. Soc.* **61** 382–91

[22] Warren B E 1969 *X-Ray Diffraction* (Reading, MA: Addison-Wesley)

[23] Wilkens M 1970 *Fundamental Aspects of Dislocation Theory (NBS Special Publication 317)* vol 2, ed J A Simmons (Washington, DC: US Government Printing Office) p 1195

[24] Krivoglaz M A 1996 *X-Ray and Neutron Diffraction in Non-Ideal Crystals* (Berlin: Springer)

[25] Warren B E and Averbach B L 1950 The effect of cold-work distortion on x-ray diffraction *J. Appl. Phys.* **21** 595–9

[26] Warren B E and Averbach B L 1952 The separation of cold-work distortion and particle size broadening in x-ray patterns *J. Appl. Phys.* **23** 497

[27] Warren B E and Averbach B L 1952 The separation of stacking fault broadening in cold-worked metals *J. Appl. Phys.* **23** 1059

[28] Klimanek P 1993 X-ray diffraction analysis of substructures in plastically deformed bcc materials *J. Physique* IV **3** 2149–54

[29] Klimanek P 1988 Möglichkeiten und Probleme der Beugungsanalyse an strukturell inhomogenen Vielkristallen *Freiberger Forschungsheft* B **265** 76–94

[30] Klimanek P 1989 Problems in diffraction analysis of real polycrystals *X-Ray and Neutron Structure Analysis in*

Materials Science ed J Hasek (New York: Plenum) pp 125–38
[31] Krivoglaz M A 1967 *Theory of X-Ray and Thermal Neutron Scattering by Real Crystals* (Moscow: Nauka) (in Russian)
[32] Krivoglaz M A 1983 *Theory of X-Ray and Neutron Diffraction by Imperfect Crystals* (Kiev: Naukova Dumka) (in Russian)
[33] Wilkens M 1970 The determination of density and distribution of dislocations in deformed single crystals from broadened x-ray diffraction profiles *Phys. Status Solidi* a **2** 359–71
[34] Klimanek P 1988 Grundlagen der Röntgenographischen Profilanalyse an realen Vielkristallen *Vorträge der 5. Tagung 'Festkörperanalytik'* (Karl-Marx-Stadt: TU Karl-Marx-Stadt) pp 310–29
[35] Byrne J G 1979 A review of positron studies of the annealing of the cold worked state *Metall. Trans.* A **10** 791–807
[36] Nabarro F R N 1976 *Theory of Crystal Dislocations* (Oxford: Oxford University Press)
[37] Hübner C H, Staab T and Krause-Rehberg R 1995 Positron diffusion in fine-grained materials—a Monte Carlo simulation *Appl. Phys.* A **61** 203–6
[38] Wellner P, Gessinger G H and Exner H-E 1974 Der Einflußdes Pressens auf die Sinterkinetik kugelförmiger Kupferteilchen *Z. Metall.* **65** 602–9
[39] Lányi P 1979 Strukturelle Aktivität und Verdichtungskinetik im Frühstadium des Schwindungsmaximums *PhD Thesis* Zentralinstitut für Festkörperphysik und Werkstofforschung, Dresden
[40] Staab T 1996 Positronenlebensdauerspektroskopieuntersuchungen zum Sinterprozeßin Metallpulverpreßlingen—Der Einflußvon Gefüge und Mikrostruktur auf den Materialtransport *PhD Thesis* Martin-Luther Universität Halle-Wittenberg
[41] Ashby M F 1974 A first report on sintering diagrams *Acta Metall.* **22** 275–89